Asociación Argentina
de Mecánica Computacional

Mecánica Computacional Vol XXVII, págs. 2397-2410 (artículo completo)
Alberto Cardona, Mario Storti, Carlos Zuppa. (Eds.)
San Luis, Argentina, 10-13 Noviembre 2008

GALERKIN BOUNDARY INTEGRAL EQUATIONS APPLIED TO THREE DIMENSIONAL STOKES FLOWS

Jorge D'Elía, Laura Battaglia, Mario A. Storti and Alberto Cardona

Centro Internacional de Métodos Computacionales en Ingeniería (CIMEC), Instituto de Desarrollo Tecnológico para la Industria Química (INTEC), Universidad Nacional del Litoral - CONICET , Güemes 3450, 3000-Santa Fe, Argentina, e-mail: lbattaglia@santafe-conicet.gov.ar, web page: http://www.cimec.org.ar

Keywords: three dimensional creeping flow, weak singularity, boundary integral equation, variational boundary element method, Galerkin boundary element method, double surface integral, Taylor scheme.

Abstract. In this work, steady creeping three dimensional flow of a viscous and incompressible fluid around closed rigid bodies is numerically solved using a Galerkin scheme applied to the Power-Miranda boundary integral equation. The related double surface integrals that account the pairwise interaction among all boundary elements are quadruple and they are computed on flat simplex triangles using the scheme proposed by Taylor (D. J. Taylor, IEEE Trans. on Antennas and Propagation, 51(7):1630–1637 (2003)). Numerical examples include the creeping steady flow around the unit sphere and the unit cube, covering issues on the convergence under mesh refinement of the numerical solution, stability under small mesh perturbations and indifference of the drag force to the direction of the incoming velocity relative to a center line of the body.

1 INTRODUCTION

Integral boundary equations are usually solved with the Boundary Element Method (BEM) (París and Cañas, 1997; Hartmann, 1989). Typically, collocation techniques are employed, for instance, for modelling Stokes flow (Power and Wrobel, 1995; Kim and Karrila, 1989) as in Fachinotti et al. (2007) where fast integration was performed using the collocation method while self-integrals, that contain singular kernels, were analytically computed over linear triangles. Another alternatives are also possible like the "Galerkin Boundary Element Method" (GBEM). When this procedure is carried with boundary elements (or panels) in $\mathbb{R}^3$ leads to compute double surface integrals, i. e. quadruple integrals, that account the pairwise interaction among all elements (or panels) of the BEM mesh, task that is carried out through a double nested element loop $p, q = 1, 2, ..., E$, where E is the number of elements in the BEM mesh. In the case of weak singular kernels, analytical expressions for double surface integrals are known for some cases, for instance, the so called "potential integrals" for linear layers on flat triangles of the Green functions for Laplace and Helmholtz equations (Eibert and Hansen, 1995; Sievers et al., 2005), in other cases a numerical quadrature is usually performed. When the generic pair p, q of interacting panels, with $p \neq q$, do not share an edge nor a vertex, its kernels are regular and a Gauss-Legendre quadrature formula is usually sufficient, otherwise there are weak singularities due to a common edge or a common vertex (Burghignoli et al., 2004). When $p = q$, both panels are coincident and, then, the whole integration domain has a weak singularity. For hand double surface integrals with flat triangular elements, Taylor (2003a) and (Taylor, 2003b) proposed a systematic way for its semi-numerical computation based on a convenient reordering of the four iterate integrations that translates the weak singularity at the origin of the $\mathbb{R}^4$ integration space and, then, a systematic use of the Duffy's transformations, i.e. using polar coordinates with the singularity at the origin, in order to regularize their integrand. In a previous work a slightly modified implementation of the Taylor scheme was presented (D'Elía and Battaglia, 2006), where a full numerical quadrature was employed in the four integration coordinates in order to handle generic Green functions with a weak singularity. In this work, the steady creeping three dimensional flow of a viscous and incompressible fluid around closed rigid bodies is numerically solved using a standard Galerkin scheme applied to the Power-Miranda boundary integral equation (Power and Miranda, 1987). The modified Taylor scheme is employed here as a "black box" for computing the double surface integrations among all triangular flat panels of the BEM mesh. Numerical examples include the creeping steady flow around the unit sphere and the unit cube, covering issues such as convergence of the numerical solution under mesh refinement and its stability under mesh perturbations. Gauss-Legendre quadrature formulas, with $2 \leq n_{1d} \leq 6$ points in each integration coordinate, and flat simplex triangles are used in all cases. Another validation for the cube case is also included by a finite element computation using the PETSc-FEM (2007) code. This procedure can be also of interest in so called Variational Boundary Element Method (VBEM) as used, for instance, in fluid-structure-interaction (Paquay, 2002) or acoustics (Schuhmacher, 2000).

2 GOVERNING EQUATIONS

For the creeping flow around a closed, rigid and piecewise smooth body surface S, the Power and Miranda (1987) alternative that allows the determination of a net force and torque on a closed body surface S by solving the modified boundary integral equation

$$\int_S dS_{\mathbf{y}} \{\mathbf{K}[\boldsymbol{\psi}(\mathbf{x}) - \boldsymbol{\psi}(\mathbf{y})] + \mathbf{P}\boldsymbol{\psi}(\mathbf{y})\} = -\mathbf{u}(\mathbf{x}) \quad \text{for } \mathbf{x} \in S; \tag{1}$$

where $\boldsymbol{\psi}$ is the surface density and $\mathbf{u}(\mathbf{x})$ is the unperturbed incoming flow velocity. The surface element is denoted as $dS_{\mathbf{y}} = dS(\mathbf{y})$, while the integration and field points are $\mathbf{y} = (y_1, y_2, y_3)$ and $\mathbf{x} = (x_1, x_2, x_3)$, respectively. The kernels $\mathbf{K} = \mathbf{K}(\mathbf{x}, \mathbf{y})$ and $\mathbf{P} = \mathbf{P}(\mathbf{x}, \mathbf{y})$ are related to double-layer surface and point sources, respectively, as follows, see Fig. 1 (left).

The double-layer surface kernel $\mathbf{K}$ is due to the surface density $\boldsymbol{\psi}$ of stresslets over the body surface (Ladyzhenskaya, 1969; Pozrikidis, 1996, 1997), and it is given by

$$K_{ij} = -\frac{3}{4\pi\mu}\frac{r_i^0\, r_j^0\, r_k^0\, n_k^0}{r^2}\ ; \tag{2}$$

$$\text{with} \quad \mathbf{r}^0 = \mathbf{r}/r \quad ; \quad \mathbf{r} = \mathbf{x} - \mathbf{y} \quad ; \quad r = \|\mathbf{x} - \mathbf{y}\|_2\ ; \tag{3}$$

where μ is the dynamic fluid viscosity, while $n_k^0 = n_k^0(\mathbf{y})$ is the unit surface normal. For smooth surfaces, this kernel has the key property

$$\int_S dS_{\mathbf{y}} \mathbf{K}_{ij}(\mathbf{x}, \mathbf{y}) = \frac{1}{2\mu}\delta_{ij} \quad ; \quad \text{for } \mathbf{x} \in S; \tag{4}$$

where δ_{ij} is the Kronecker delta. On the other hand, the point kernel $\mathbf{P}$ is due to a combined pair of Stokeslet and a rotlet point singularities, and it gives rise to a force and a torque when the combined kernel is integrated over a closed surface that encloses it. Their approach is an extension to the steady Stokes equation of the Mikhlin results on the exterior Dirichlet problem for the Laplace equation (Mikhlin, 1965, 1970). A key idea of the Power-Miranda scheme is to choose that the strength of the point (combined) kernel depends linearly upon the surface density $\boldsymbol{\psi}(\mathbf{y})$, i.e.,

$$\mathbf{P}(\mathbf{x}, \mathbf{y}) = \mathbf{C}(\mathbf{x}, \mathbf{y})\boldsymbol{\psi}(\mathbf{y})\ ; \tag{5}$$

where the coupled matrix $\mathbf{C} = \mathbf{C}(\mathbf{x}, \mathbf{y})$, after some algebra, can be written as

$$\mathbf{C} = \frac{1}{8\pi\mu R^3}\int_S dS_{\mathbf{y}}(\mathbf{S} + \mathbf{R})\ ; \tag{6}$$

with its Stokeslet part

$$\mathbf{S} = \begin{bmatrix} (x_1x_1 + R^2) & x_1x_2 & x_1x_3 \\ x_2x_3 & (x_2x_2 + R^2) & x_2x_3 \\ x_3x_1 & x_3x_2 & (x_3x_3 + R^2) \end{bmatrix} \quad ; \tag{7}$$

and its rotlet one

$$\mathbf{R} = \begin{bmatrix} (y_2x_2 + y_3x_3) & -y_1x_2 & -y_1x_3 \\ -y_2x_1 & (y_3x_3 + y_1x_1) & -y_2x_3 \\ -y_3x_1 & -y_3x_2 & (y_1x_1 + y_2x_2) \end{bmatrix}\ ; \tag{8}$$

where $R = \|\mathbf{x}\|_2$ when, for simplicity, the point singularity is placed at the origin, with the origin inside the closed body. It should be noticed that the coupled matrix $\mathbf{C}$ given by Eqs. (5-8), in these conditions, is always regular. Reordering terms in Eq. (1),

$$\int_S dS_{\mathbf{y}}\{(\mathbf{P} - \mathbf{K})\boldsymbol{\psi}(\mathbf{y}) + \mathbf{K}\boldsymbol{\psi}(\mathbf{x})\} = -\mathbf{u}(\mathbf{x}) \quad \text{for } \mathbf{x} \in S; \tag{9}$$

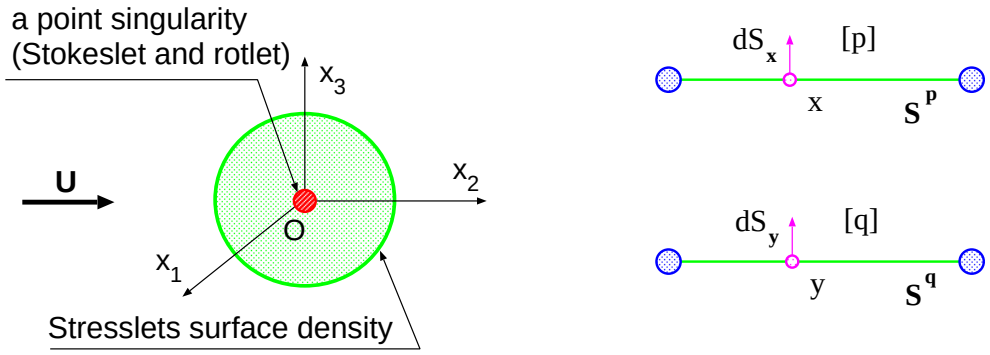

Figure 1: Left: a closed, rigid and piecewise smooth body surface S with a surface density of Stresslets, and a point singularity (Stokeslet and rotlet) inside S. Right: the $\mathbf{x}, \mathbf{y}$ points related to the p, q panels, respectively, for the double nested loop $p, q = 1, 2, ..., E$.

that is

$$\int_S dS_{\mathbf{y}} \{\mathbf{A}\boldsymbol{\psi}(\mathbf{y}) + \mathbf{K}\boldsymbol{\psi}(\mathbf{x})\} = -\mathbf{u}(\mathbf{x}) \quad \text{for } \mathbf{x} \in S; \tag{10}$$

where $\mathbf{A} = \mathbf{A}(\mathbf{x}, \mathbf{y})$ is the difference between both kernels $\mathbf{A} = \mathbf{P} - \mathbf{K}$. Then, the Power-Miranda alternative can be written as $\mathbf{I}(\mathbf{x}) = -\mathbf{u}(\mathbf{x})$ for $\mathbf{x} \in S$, with the integral operator

$$\mathbf{I}(\mathbf{x}) \equiv \int_S dS_{\mathbf{y}} \{\mathbf{A}\boldsymbol{\psi}(\mathbf{y}) + \mathbf{K}\boldsymbol{\psi}(\mathbf{x})\} \, . \tag{11}$$

3 NUMERICAL FORMULATIONS

Two numerical formulations are considered in this work. First, a collocation technique (Becker, 1992) is employed and, next, a Galerkin one. The collocation algebra is later employed for checking the corresponding Galerkin procedure. Numerical results were found through both methods but, due to space reasons, only those obtained with the GBEM alternative are reported. These techniques use a double nested loop over the panels $p, q = 1, 2, ..., E$, where the $\mathbf{x}$ and $\mathbf{y}$ points are related to the p, q panels, respectively, see Fig. 1 (right). The assembling process is performed in each case by nodes or by elements through a simple and rather "obvious" example in $\mathbb{R}^2$, as shown in Fig. 2, with $E = 3$ boundary elements and $N = 4$ nodes. Element and nodal values are denoted with supra and sub index, respectively. Finally. integration overt triangles is summarized.

3.1 Collocation through an element assembling

Assuming a constant density layer $\boldsymbol{\psi}(\mathbf{y})$ on the surface of each panel, it can be extracted out of the surface integrals in Eq. (10). In the "obvious" example $p, q = 1, 2, 3$, the collocation technique results in the following system of equations

$$[\mathbf{A}^{11}\boldsymbol{\psi}^1 + \mathbf{K}^{11}\boldsymbol{\psi}^1] + [\mathbf{A}^{12}\boldsymbol{\psi}^2 + \mathbf{K}^{12}\boldsymbol{\psi}^1] + [\mathbf{A}^{13}\boldsymbol{\psi}^3 + \mathbf{K}^{13}\boldsymbol{\psi}^1] = -\mathbf{u}^1 \, ; \tag{12}$$

$$[\mathbf{A}^{21}\boldsymbol{\psi}^1 + \mathbf{K}^{21}\boldsymbol{\psi}^2] + [\mathbf{A}^{22}\boldsymbol{\psi}^2 + \mathbf{K}^{22}\boldsymbol{\psi}^2] + [\mathbf{A}^{23}\boldsymbol{\psi}^3 + \mathbf{K}^{23}\boldsymbol{\psi}^2] = -\mathbf{u}^2 \, ; \tag{13}$$

$$[\mathbf{A}^{31}\boldsymbol{\psi}^1 + \mathbf{K}^{31}\boldsymbol{\psi}^3] + [\mathbf{A}^{32}\boldsymbol{\psi}^2 + \mathbf{K}^{32}\boldsymbol{\psi}^3] + [\mathbf{A}^{33}\boldsymbol{\psi}^3 + \mathbf{K}^{33}\boldsymbol{\psi}^3] = -\mathbf{u}^3 \, ; \tag{14}$$

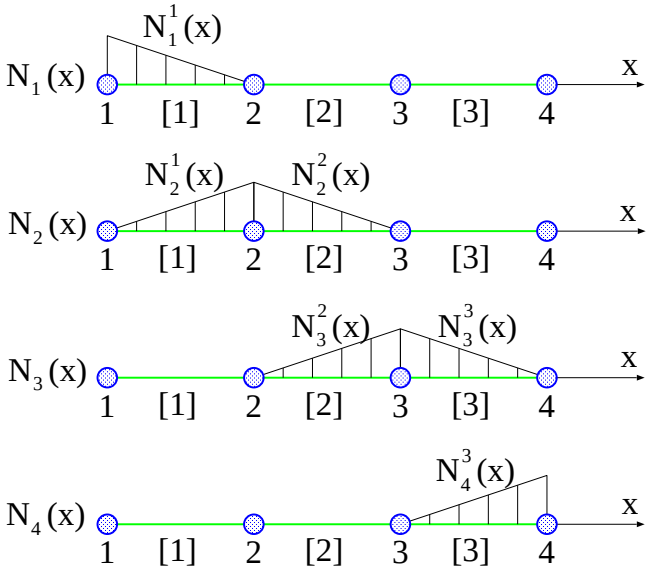

Figure 2: Scketch of an "obvious" GBEM mesh in $\mathbb{R}^2$ with $E = 3$ boundary elements and $N = 4$ nodes.

for the surface density $\boldsymbol{\psi} = (\boldsymbol{\psi}^1, \boldsymbol{\psi}^2, \boldsymbol{\psi}^3)$, where $\mathbf{A}^{pq} = \mathbf{A}(\mathbf{x}^p, \mathbf{y}^q)$, $\mathbf{u}^p = \mathbf{u}(\mathbf{x}^p)$ and $\boldsymbol{\psi}^p = \boldsymbol{\psi}(\mathbf{x}^p)$ are evaluated at the panel centroids $\mathbf{x}^p$. Re-ordering

$$\begin{bmatrix} \tilde{\mathbf{A}}^{11} & \mathbf{A}^{12} & \mathbf{A}^{13} \\ \mathbf{A}^{21} & \tilde{\mathbf{A}}^{22} & \mathbf{A}^{23} \\ \mathbf{A}^{31} & \mathbf{A}^{32} & \tilde{\mathbf{A}}^{33} \end{bmatrix} \begin{bmatrix} \boldsymbol{\psi}^1 \\ \boldsymbol{\psi}^2 \\ \boldsymbol{\psi}^3 \end{bmatrix} = \begin{bmatrix} -\mathbf{u}^1 \\ -\mathbf{u}^2 \\ -\mathbf{u}^3 \end{bmatrix} \; ; \tag{15}$$

where

$$\tilde{\mathbf{A}}^{11} = \mathbf{A}^{11} + (\mathbf{K}^{11} + \mathbf{K}^{12} + \mathbf{K}^{13}) \; ; \tag{16}$$

$$\tilde{\mathbf{A}}^{22} = \mathbf{A}^{22} + (\mathbf{K}^{21} + \mathbf{K}^{22} + \mathbf{K}^{23}) \; ; \tag{17}$$

$$\tilde{\mathbf{A}}^{33} = \mathbf{A}^{33} + (\mathbf{K}^{31} + \mathbf{K}^{32} + \mathbf{K}^{33}) \; ; \tag{18}$$

and a numerical solution of Eq. (15) gives the surface density $\boldsymbol{\psi} = (\boldsymbol{\psi}^1, \boldsymbol{\psi}^2, \boldsymbol{\psi}^3)$.

3.2 Galerkin approximation through a nodal assembling

In this section, Eq. (10) is solved by a Galerkin technique in the context of a standard Finite Element Method (FEM). As already stated in the introduction, in the present work it will be only assumed the case of a linear density layer $\boldsymbol{\psi}(\mathbf{y})$ on the surface of each panel which is a simplex element. As first step, the nodal shape functions are decomposed as the sum of its elemental contributions, see Fig. 2,

$$\mathbf{N}_1(\mathbf{x}) = \mathbf{N}_1^1(\mathbf{x}) \; ; \tag{19}$$

$$\mathbf{N}_2(\mathbf{x}) = \mathbf{N}_2^1(\mathbf{x}) + \mathbf{N}_2^2(\mathbf{x}) \; ; \tag{20}$$

$$\mathbf{N}_3(\mathbf{x}) = \mathbf{N}_3^2(\mathbf{x}) + \mathbf{N}_3^3(\mathbf{x}) \; ; \tag{21}$$

$$\mathbf{N}_4(\mathbf{x}) = \mathbf{N}_4^3(\mathbf{x}) \; ; \tag{22}$$

and the same for the incoming velocity field

$$\mathbf{u}_1(\mathbf{x}) = \mathbf{u}_1^1(\mathbf{x}) \; ; \tag{23}$$
$$\mathbf{u}_2(\mathbf{x}) = \mathbf{u}_2^1(\mathbf{x}) + \mathbf{u}_2^2(\mathbf{x}) \; ; \tag{24}$$
$$\mathbf{u}_3(\mathbf{x}) = \mathbf{u}_3^2(\mathbf{x}) + \mathbf{u}_3^3(\mathbf{x}) \; ; \tag{25}$$
$$\mathbf{u}_4(\mathbf{x}) = \mathbf{u}_4^3(\mathbf{x}) \; ; \tag{26}$$

where, as usual,

$$\mathbf{u}^1(\mathbf{x}) = \mathbf{N}^1(\mathbf{x})\mathbf{U}^1 \; ; \tag{27}$$
$$\mathbf{u}^2(\mathbf{x}) = \mathbf{N}^2(\mathbf{x})\mathbf{U}^2 \; ; \tag{28}$$
$$\mathbf{u}^3(\mathbf{x}) = \mathbf{N}^3(\mathbf{x})\mathbf{U}^3 \; ; \tag{29}$$

with the row vectors

$$\mathbf{N}^1(\mathbf{x}) = \begin{bmatrix} N_1^1(\mathbf{x}) & N_2^1(\mathbf{x}) \end{bmatrix} \; ; \tag{30}$$
$$\mathbf{N}^2(\mathbf{x}) = \begin{bmatrix} N_2^2(\mathbf{x}) & N_3^2(\mathbf{x}) \end{bmatrix} \; ; \tag{31}$$
$$\mathbf{N}^3(\mathbf{x}) = \begin{bmatrix} N_3^3(\mathbf{x}) & N_4^3(\mathbf{x}) \end{bmatrix} \; ; \tag{32}$$

and the column ones

$$\mathbf{U}^1 = \begin{bmatrix} U_1 \\ U_2 \end{bmatrix} \; ; \quad \mathbf{U}^2 = \begin{bmatrix} U_2 \\ U_3 \end{bmatrix} \; ; \quad \mathbf{U}^3 = \begin{bmatrix} U_3 \\ U_4 \end{bmatrix} \; . \tag{33}$$

The Galerkin technique in the present context chooses the nodal shape functions $\mathbf{N}_i(\mathbf{x})$ to enforce the orthogonality conditions

$$\int_S dS_{\mathbf{x}} \overline{\mathbf{N}}_i(\mathbf{x})\mathbf{I}(\mathbf{x}) + \int_S dS_{\mathbf{x}} \overline{\mathbf{N}}_i(\mathbf{x})\mathbf{u}(\mathbf{x}) = \mathbf{0} \; ; \tag{34}$$

for $i = 1, 2, ..., N$, where $\overline{\mathbf{N}}_i = \mathbf{N}_i^T$ (transposed). In the example, using firstly a FEM nodal assembling, Eq. (34) is split as

$$\int_S dS_{\mathbf{x}} \overline{\mathbf{N}}_1(\mathbf{x})\mathbf{I}(\mathbf{x}) = -\int_S dS_{\mathbf{x}} \overline{\mathbf{N}}_1(\mathbf{x})\mathbf{u}(\mathbf{x}) \; ; \tag{35}$$
$$\int_S dS_{\mathbf{x}} \overline{\mathbf{N}}_2(\mathbf{x})\mathbf{I}(\mathbf{x}) = -\int_S dS_{\mathbf{x}} \overline{\mathbf{N}}_2(\mathbf{x})\mathbf{u}(\mathbf{x}) \; ; \tag{36}$$
$$\int_S dS_{\mathbf{x}} \overline{\mathbf{N}}_3(\mathbf{x})\mathbf{I}(\mathbf{x}) = -\int_S dS_{\mathbf{x}} \overline{\mathbf{N}}_3(\mathbf{x})\mathbf{u}(\mathbf{x}) \; ; \tag{37}$$
$$\int_S dS_{\mathbf{x}} \overline{\mathbf{N}}_4(\mathbf{x})\mathbf{I}(\mathbf{x}) = -\int_S dS_{\mathbf{x}} \overline{\mathbf{N}}_4(\mathbf{x})\mathbf{u}(\mathbf{x}) \; ; \tag{38}$$

and replacing Eq. (19-22) into Eq. (34), the last one can be written as the sum of the elemental contributions

$$\int_S dS_{\mathbf{x}} \overline{\mathbf{N}}_1^1(\mathbf{x})\mathbf{I}(\mathbf{x}) = \mathbf{b}_1 \; ; \tag{39}$$
$$\int_S dS_{\mathbf{x}} \overline{\mathbf{N}}_2^1(\mathbf{x})\mathbf{I}(\mathbf{x}) + \int_S dS_{\mathbf{x}} \overline{\mathbf{N}}_2^2(\mathbf{x})\mathbf{I}(\mathbf{x}) = \mathbf{b}_2 \; ; \tag{40}$$
$$\int_S dS_{\mathbf{x}} \overline{\mathbf{N}}_3^2(\mathbf{x})\mathbf{I}(\mathbf{x}) + \int_S dS_{\mathbf{x}} \overline{\mathbf{N}}_3^3(\mathbf{x})\mathbf{I}(\mathbf{x}) = \mathbf{b}_3 \; ; \tag{41}$$
$$\int_S dS_{\mathbf{x}} \overline{\mathbf{N}}_4^3(\mathbf{x})\mathbf{I}(\mathbf{x}) = \mathbf{b}_4 \; ; \tag{42}$$

where the source term $\mathbf{b} = (\mathbf{b}_1, \mathbf{b}_2, \mathbf{b}_3, \mathbf{b}_4)$ is also computed by adding the elemental contributions

$$\mathbf{b}_1 = -\int_S dS_{\mathbf{x}} \overline{\mathbf{N}}_1^1(\mathbf{x}) \mathbf{u}^1(\mathbf{x}) \; ; \tag{43}$$

$$\mathbf{b}_2 = -\int_S dS_{\mathbf{x}} \overline{\mathbf{N}}_2^1(\mathbf{x}) \mathbf{u}^1(\mathbf{x}) - \int_S dS_{\mathbf{x}} \overline{\mathbf{N}}_2^2(\mathbf{x}) \mathbf{u}^2(\mathbf{x}) \; ; \tag{44}$$

$$\mathbf{b}_3 = -\int_S dS_{\mathbf{x}} \overline{\mathbf{N}}_3^2(\mathbf{x}) \mathbf{u}^2(\mathbf{x}) - \int_S dS_{\mathbf{x}} \overline{\mathbf{N}}_3^3(\mathbf{x}) \mathbf{u}^3(\mathbf{x}) \; ; \tag{45}$$

$$\mathbf{b}_4 = -\int_S dS_{\mathbf{x}} \overline{\mathbf{N}}_4^3(\mathbf{x}) \mathbf{u}^3(\mathbf{x}) \; . \tag{46}$$

3.3 Galerkin approximation through an element assembling

Due to the fully coupled nature of the term $\mathbf{I}(\mathbf{x})$ in Eq. (11), from now on it will be more convenient to shift to an element assembling. Then, Eq. (34) is rewritten as the sum of the contributions of the three boundary elements

$$\int_{S^1} dS_{\mathbf{x}} \overline{\mathbf{N}}^1(\mathbf{x}) \mathbf{I}(\mathbf{x}) + \int_{S^2} dS_{\mathbf{x}} \overline{\mathbf{N}}^2(\mathbf{x}) \mathbf{I}(\mathbf{x}) + \int_{S^3} dS_{\mathbf{x}} \overline{\mathbf{N}}^3(\mathbf{x}) \mathbf{I}(\mathbf{x}) = \tag{47}$$

$$-\int_{S^1} dS_{\mathbf{x}} \overline{\mathbf{N}}^1(\mathbf{x}) \mathbf{u}^1(\mathbf{x}) - \int_{S^2} dS_{\mathbf{x}} \overline{\mathbf{N}}^2(\mathbf{x}) \mathbf{u}^2(\mathbf{x}) - \int_{S^3} dS_{\mathbf{x}} \overline{\mathbf{N}}^3(\mathbf{x}) \mathbf{u}^3(\mathbf{x}) \; . \tag{48}$$

The $\mathbf{I}(\mathbf{x})$ integral is also decomposed as the sum of the contributions of the three elements

$$\mathbf{I}(\mathbf{x}) = \mathbf{I}^1(\mathbf{x}) + \mathbf{I}^2(\mathbf{x}) + \mathbf{I}^3(\mathbf{x}) \; ; \tag{49}$$

where

$$\mathbf{I}^1(\mathbf{x}) = \int_{S^1} dS_{\mathbf{y}} \{ \mathbf{A} \boldsymbol{\psi}^1(\mathbf{y}) + \mathbf{K} [\boldsymbol{\psi}^1(\mathbf{x}) + \boldsymbol{\psi}^2(\mathbf{x}) + \boldsymbol{\psi}^3(\mathbf{x})] \} \; ; \tag{50}$$

$$\mathbf{I}^2(\mathbf{x}) = \int_{S^2} dS_{\mathbf{y}} \{ \mathbf{A} \boldsymbol{\psi}^2(\mathbf{y}) + \mathbf{K} [\boldsymbol{\psi}^1(\mathbf{x}) + \boldsymbol{\psi}^2(\mathbf{x}) + \boldsymbol{\psi}^3(\mathbf{x})] \} \; ; \tag{51}$$

$$\mathbf{I}^3(\mathbf{x}) = \int_{S^3} dS_{\mathbf{y}} \{ \mathbf{A} \boldsymbol{\psi}^3(\mathbf{y}) + \mathbf{K} [\boldsymbol{\psi}^1(\mathbf{x}) + \boldsymbol{\psi}^2(\mathbf{x}) + \boldsymbol{\psi}^3(\mathbf{x})] \} \; . \tag{52}$$

Taking into account the compact nature of the shape functions $\mathbf{N}^p(\mathbf{x})$, "hat" functions in the present case, after some algebra, results the system equation

$$\mathbf{H} \boldsymbol{\Psi} = \mathbf{b} \; ; \tag{53}$$

with the sub-blocks

$$\mathbf{H} = \begin{bmatrix} \mathbf{H}_{11} & \mathbf{H}_{12} & \mathbf{H}_{13} \\ \mathbf{H}_{21} & \mathbf{H}_{22} & \mathbf{H}_{23} \\ \mathbf{H}_{31} & \mathbf{H}_{32} & \mathbf{H}_{33} \end{bmatrix} \; ; \quad \boldsymbol{\Psi} = \begin{bmatrix} \boldsymbol{\psi}^1 \\ \boldsymbol{\psi}^2 \\ \boldsymbol{\psi}^3 \end{bmatrix} \; ; \quad \mathbf{b} = \begin{bmatrix} \mathbf{b}^1 \\ \mathbf{b}^2 \\ \mathbf{b}^3 \end{bmatrix} \; . \tag{54}$$

Introducing the short notation

$$\mathcal{I}^{pq}\{...\} = \int_{S^p} dS_{\mathbf{x}} \int_{S^q} dS_{\mathbf{y}} \; \overline{\mathbf{N}}^p(\mathbf{x}) \; \{...\} \; \mathbf{N}^q(\mathbf{y}) \; ; \tag{55}$$

incoming flow	unperturbed velocity	force $\mathbf{F}$	torque $\mathbf{T}$
uniform	$(U,0,0)$	$6\pi\mu UR\,\mathbf{e}_1^0$	$\mathbf{0}$
shear	$U(x_2,-x_1,0)$	$\mathbf{0}$	$8\pi\mu UR^2\,\mathbf{e}_3^0$
paraboloidal	$U(x_1^2+x_2^2,0,0)$	$4\pi\mu UR\,\mathbf{e}_1^0$	$\mathbf{0}$

Table 1: Steady creeping flow around a sphere. Analytical expressions for the viscous force and torque.

for the double surface integrals, with $p,q=1,2,...,E$, the entries of the system matrix $\mathbf{H}$ are for its first row

$$\mathbf{H}_{11}=\mathcal{I}^{11}\{\mathbf{A}\}+\mathcal{I}^{11}\{\mathbf{K}\}+\mathcal{I}^{12}\{\mathbf{K}\}+\mathcal{I}^{13}\{\mathbf{K}\}\;; \tag{56}$$
$$\mathbf{H}_{12}=\mathcal{I}^{12}\{\mathbf{A}\}\;; \tag{57}$$
$$\mathbf{H}_{13}=\mathcal{I}^{13}\{\mathbf{A}\}\;; \tag{58}$$

for its second row

$$\mathbf{H}_{21}=\mathcal{I}^{21}\{\mathbf{A}\}\;; \tag{59}$$
$$\mathbf{H}_{22}=\mathcal{I}^{22}\{\mathbf{A}\}+\mathcal{I}^{21}\{\mathbf{K}\}+\mathcal{I}^{22}\{\mathbf{K}\}+\mathcal{I}^{23}\{\mathbf{K}\}\;; \tag{60}$$
$$\mathbf{H}_{23}=\mathcal{I}^{23}\{\mathbf{A}\}\;; \tag{61}$$

and for its third row

$$\mathbf{H}_{31}=\mathcal{I}^{31}\{\mathbf{A}\}\;; \tag{62}$$
$$\mathbf{H}_{32}=\mathcal{I}^{32}\{\mathbf{A}\}\;; \tag{63}$$
$$\mathbf{H}_{33}=\mathcal{I}^{33}\{\mathbf{A}\}+\mathcal{I}^{31}\{\mathbf{K}\}+\mathcal{I}^{32}\{\mathbf{K}\}+\mathcal{I}^{33}\{\mathbf{K}\}\;. \tag{64}$$

A first check between the entries of the system matrix obtained by the collocation procedure and the Galerkin one, Eq. (15-18) and Eq. (56-64), respectively, reveals that they have the same algebraic form. On the other hand, the element source vectors are computed as the matrix-vector products

$$\mathbf{b}^1=\mathbf{M}^1\mathbf{U}^1\;;\quad \mathbf{b}^2=\mathbf{M}^2\mathbf{U}^2\;;\quad \mathbf{b}^3=\mathbf{M}^3\mathbf{U}^3\;; \tag{65}$$

between the "mass" like matrix, given by the single surface integrals

$$\mathbf{M}^1=-\int_{S^1}dS_{\mathbf{x}}\overline{\mathbf{N}}^1(\mathbf{x})\mathbf{N}^1(\mathbf{x})\;; \tag{66}$$
$$\mathbf{M}^2=-\int_{S^2}dS_{\mathbf{x}}\overline{\mathbf{N}}^2(\mathbf{x})\mathbf{N}^2(\mathbf{x})\;; \tag{67}$$
$$\mathbf{M}^3=-\int_{S^3}dS_{\mathbf{x}}\overline{\mathbf{N}}^3(\mathbf{x})\mathbf{N}^3(\mathbf{x})\;; \tag{68}$$

and the unperturbed velocities $\mathbf{U}^1$, $\mathbf{U}^2$ and $\mathbf{U}^3$. This "obvious" example in $\mathbb{R}^2$ is sufficient to shows the main features of the assembling process using the Galerkin alternative, which are commons with the practical $\mathbb{R}^3$ case.

3.4 Double surface integrals over flat triangles

The double surface integral

$$\mathbf{Z}=\int_{S^p}dS_{\mathbf{x}}\int_{S^q}dS_{\mathbf{y}}\;\mathbf{F}(\mathbf{x},\mathbf{y})\;; \tag{69}$$

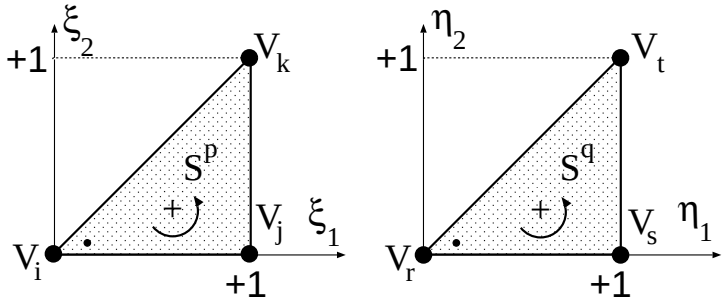

Figure 3: Unitary master triangles on the p and q panels.

is performed over the p and q panels, so it is a quadruple integral. Many times, its integrand contains the kernel $\mathbf{F} = \mathbf{QG}$, where $\mathbf{Q} = \mathbf{Q}(\mathbf{x}, \mathbf{y})$ is some multiplicative regular function and $\mathbf{G} = \mathbf{G}(r)$ is a Green function with $r = \|\mathbf{x} - \mathbf{y}\|_2$ such that it has a weak singularity $O(1/r)$. Then, Eq. (69) is transformed by using two simplex coordinate sets, i.e. (ξ_1, ξ_2) over the p panel and (η_1, η_2) over the q one,

$$(\xi_1, \xi_2) : 0 \leq \xi_1 \leq 1 \; ; \; 0 \leq \xi_2 \leq \xi_1 \; ; \tag{70}$$

$$(\eta_1, \eta_2) : 0 \leq \eta_1 \leq 1 \; ; \; 0 \leq \eta_2 \leq \eta_1 \; ; \tag{71}$$

see Fig. 3. The generic points on each of these triangles are transformed to the p and q panels using

$$\mathbf{x}(\xi_1, \xi_2) = \mathbf{N}^p(\xi_1, \xi_2)\mathbf{V}^p \; ; \tag{72}$$

$$\mathbf{y}(\eta_1, \eta_2) = \mathbf{N}^q(\eta_1, \eta_2)\mathbf{V}^q \; ; \tag{73}$$

with the element shape functions

$$\mathbf{N}^p(\xi_1, \xi_2) = \begin{bmatrix} (1 - \xi_1) & (\xi_1 - \xi_2) & \xi_2 \end{bmatrix} \; ; \tag{74}$$

$$\mathbf{N}^q(\eta_1, \eta_2) = \begin{bmatrix} (1 - \eta_1) & (\eta_1 - \eta_2) & \eta_2 \end{bmatrix} \; ; \tag{75}$$

and the element nodal coordinates in triangle vertex

$$\mathbf{V}^p = \begin{bmatrix} \mathbf{V}_i \\ \mathbf{V}_j \\ \mathbf{V}_k \end{bmatrix} \quad ; \quad \mathbf{V}^q = \begin{bmatrix} \mathbf{V}_r \\ \mathbf{V}_s \\ \mathbf{V}_t \end{bmatrix} \; . \tag{76}$$

Then, Eq. (69) is written as

$$\mathbf{Z} = \int_{S^p} dS_{\mathbf{x}} \int_{S^q} dS_{\mathbf{y}} \; \mathbf{F}(\mathbf{x}, \mathbf{y}) = J^p J^q \; \tilde{\mathbf{F}} \; ; \tag{77}$$

where $J^{p,q} = 2A^{p,q}$ are the Jacobians of each panel, and $A^{p,q}$ are its areas, respectively, and

$$\tilde{\mathbf{F}} = \int_0^1 d\xi_1 \int_0^{\xi_1} d\xi_2 \int_0^1 d\eta_1 \int_0^{\eta_1} d\eta_2 \; \mathbf{F}(\boldsymbol{\xi}, \boldsymbol{\eta}) \; . \tag{78}$$

Further details about this "dirty job" can be found in Taylor (2003a) or D'Elía and Battaglia (2006).

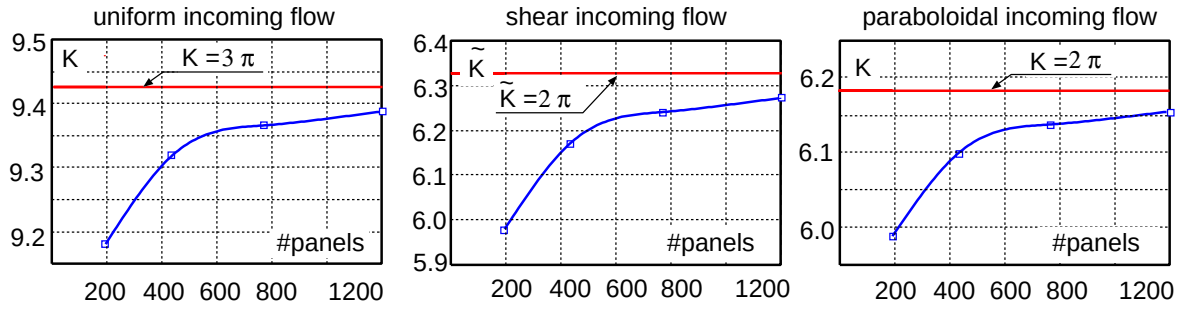

Figure 4: Creeping steady flow around the unit sphere at $\mathrm{Re} = 0.01$: convergence of the drag coefficients $K = F/(\mu U L)$ and $\tilde{K} = T/(\mu U L^2)$ with respect to mesh refinement for three incoming flow profiles.

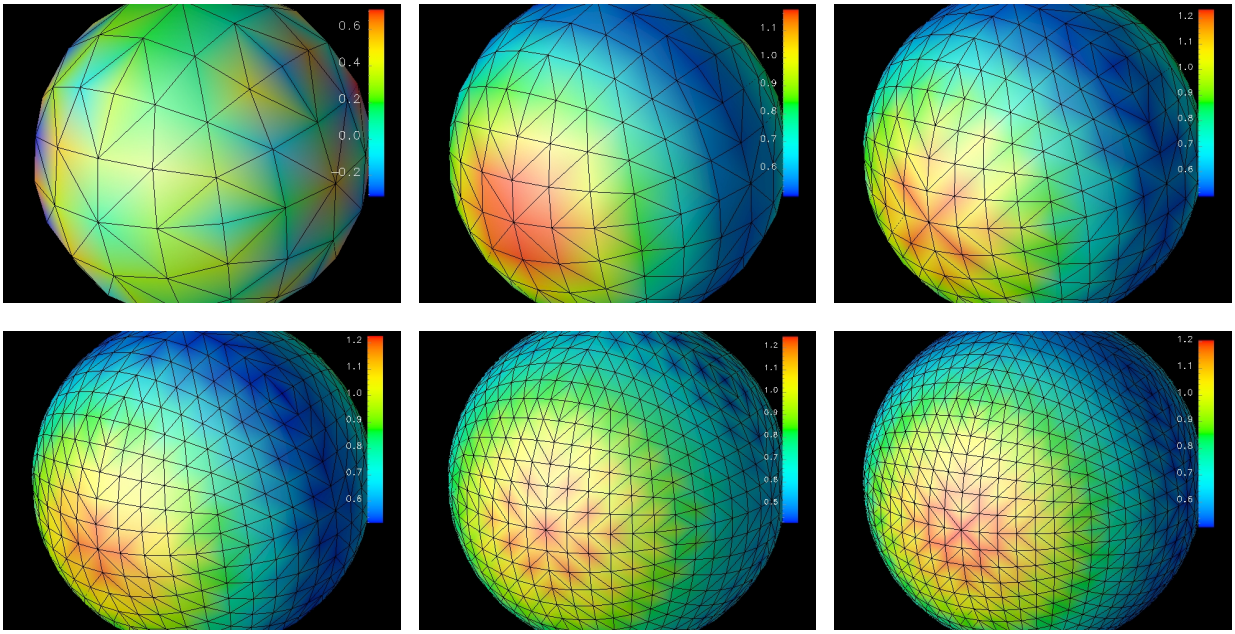

Figure 5: Convergence under mesh refinement. Isosurfaces of the t_x traction coefficient with smoothed BEM meshes for 192, 432, 768, 1200, 1728 and 2352 panels, from up to bottom and from left to right, respectively.

4 NUMERICAL EXAMPLES

Numerical simulations are performed with the proposed scheme for the steady creeping flow of a viscous and incompressible fluid around single bodies. Two cases are considered, a unit sphere and a unit cube whose centers are placed at the origin in $\mathbb{R}^3$. The numerical examples cover issues of convergence of the numerical solution under mesh refinement, its stability under small mesh perturbations and indifference of the drag force to the direction of the incoming velocity relative to a center line of the body. Gauss-Legendre quadrature formula is employed in the Taylor "black box" integrator, with $n_{1d} = 2, 3, 4, 5, 6$ Gauss Legendre quadrature points in each coordinate, and flat simplex triangles are employed in all cases.

4.1 Steady creeping flow

As it is known, steady creeping flow is restricted to fluid flow problems when the Reynolds numbers $\mathrm{Re} = UL/\nu$ are lower than one, where U and L are typical speed and length scales, while ν and $\mu = \rho\nu$ are the fluid kinematic and dynamic viscosities, respectively, and ρ is the fluid density. In this case, the body force $\mathbf{F} = (F_x, F_y, F_z)$ and body torque $\mathbf{T} = (T_x, T_y, T_z)$

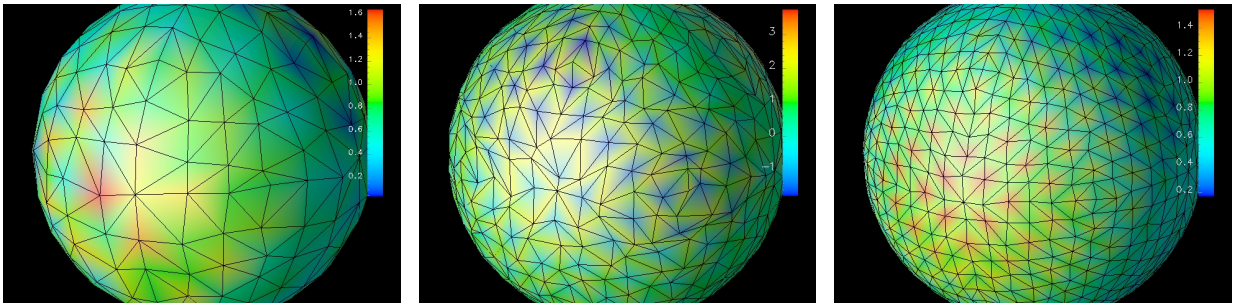

Figure 6: Isosurfaces of the t_x traction coefficient on the sphere surface with perturbed BEM meshes and a GBEM computation for 768, 1200 and 1728 panels, and 5 Gauss-Legendre quadrature points, from left to right, respectively.

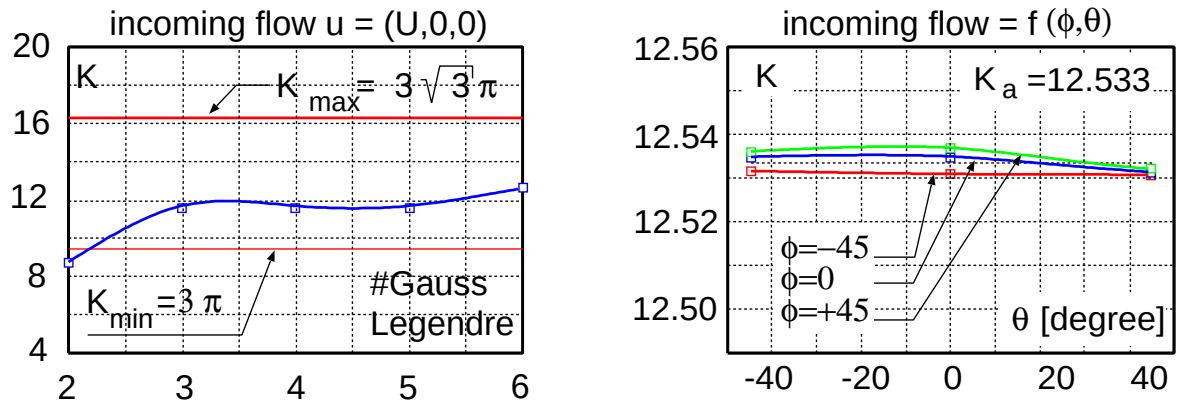

Figure 7: Creeping steady flow around the unit cube at $\mathrm{Re} = 0.01$. Convergence of the drag coefficient K with respects to the number of Gauss Legendre points (left). Indifference test of the drag coefficient K with respects to the direction of the incoming velocity $\mathbf{U} = (u_1, u_2, u_3)$, using $n_{1d} = 6$ Gauss-Legendre points (right).

are given by the surface integrals

$$\mathbf{F} = \int_{S_y} dS_{\mathbf{y}} \boldsymbol{\psi} \; ; \tag{79}$$

$$\mathbf{T} = \int_{S_y} dS_{\mathbf{y}} (\mathbf{r} \times \boldsymbol{\psi}) \; . \tag{80}$$

The drag coefficients are computed as $K = F_x/(\mu U L)$ and $\tilde{K} = T_x/(\mu U L^2)$, where $L = 2R$, the sphere diameter, or $L = A$, the cube edge length, respectively, while the traction is adimensionalized with $\mathbf{t} = \boldsymbol{\psi}/(\mu U L)$.

4.2 Sphere

The sphere case is chosen since there are analytical solutions for the force and torque for several inflow conditions. In particular, three inflow conditions are considered: uniform, shear and paraboloidal. The expressions for the unperturbed velocity, force and torque for each case are summarized in Table 1. The following values are adopted in the numerical simulations: fluid density $\rho = 1$ kg/m^3, kinematic viscosity $\nu = 2$ m^2/s, incoming speed $U = 0.01$ m/s and sphere radius $R = 1$ m. Then, the typical length is $L = 2R = 2$ m. The plots in Fig. 4 show the convergence of the drag coefficients K and $\tilde{K}$ with respect to mesh refinement for incoming flow profiles: uniform (left), shear (center) and paraboloidal (right).

The analytical traction field on the surface sphere under uniform flow is the constant value $\boldsymbol{\sigma} = (3/2)\mu U/R\ \mathbf{e}_1^0$, given the related traction coefficient $K = 3/4$, where $\mathbf{e}_1^0$ is the unit Cartesian vector in the x_1 direction. Figure 5 shows the isosurfaces of the t_x traction coefficient on the sphere surface and smooth BEM meshes for 192, 432, 768, 1200, 1728 and 2352 panels, respectively. Figure 6 is the same as previous one but with perturbed BEM meshes, of 768, 1200 and 1728 panels, respectively, in order to check the stability of the numerical solution. The mesh perturbations are performed through small random increments for the nodal positions but without leaving the sphere surface.

4.3 Cube flow case with GBEM

The cube case is selected as a very crude simplification of MEMS geometries although there is not analytical solution in this case, but bounds and semi numerical or experimental values are taken as a reference. For instance, an open interval bound is known for the drag force and it is given by $F_{\min} < F < F_{\max}$, with $F_{\min} = 3\pi\mu U A$ and $F_{\max} = \sqrt{3}F_{\min}$, where A is the cube edge length, or expressed as a drag coefficient interval, $K_{\min} < K < K_{\max}$, with $K_{\min} = 3\pi$ and $K_{\max} = 3\sqrt{3}\pi$. In the numerical simulations, the following values are adopted: fluid density $\rho = 1\ \mathrm{kg/m^3}$, kinematic viscosity $\nu = 1\ \mathrm{m^2/s}$, incoming speed $U = 0.01$ m/s and edge length $A = 1$ m. Thus, the typical length is $L = A = 1$ m. Figure 7 (left) shows the convergence of the drag coefficient K with respect to the number of Gauss-Legendre quadrature points n_{1d} in each integration coordinate. It should be noted that as the GBEM implies double surface integration, there are a total number of n_{1d}^4 quadrature points. On the other hand, in steady creeping flow, indifference of the drag force with respect to the direction of the incoming velocity related to some body axis should be verified. Figure 7 (right) shows the drag coefficient K, obtained using $n_{1d} = 6$ Gauss-Legendre points, as a function of the incoming velocity $\mathbf{U} = (u_1, u_2, u_3)$, when $u_1 = \cos(\theta)\cos(\phi)$, $u_2 = \cos(\theta)\sin(\phi)$ and $u_3 = \sin(\theta)$, for $-\pi/4 \leq \phi, \theta \leq \pi/4$, with angular steps $\Delta\phi = \Delta\theta = \pi/4$, in the spherical coordinates $0 \leq \phi < 2\pi$ and $\pi/2 \leq \theta \leq \pi/2$. From these results we can take an average value of $K_a = 12.53$.

4.4 Cube flow case with FEM

FEM computations have been performed with the open source PETSc-FEM code. This code solves the Navier-Stokes equations with the SUPG+PSPG algorithm (Tezduyar et al., 1992; Sonzogni et al., 2000), i.e. using equal-order interpolations with the PSPG stabilization term in order to bypass the Brezzi-Babuska condition. The FEM computation does include the inertial terms, so that in order to compare with the GBEM results a low Reynolds number must be chosen. The Reynolds number was set to 0.001 by choosing the particular combination of parameters $\nu = 0.1$, $U_\infty = 10^{-4}$ and $L = 1$. The flow is aligned with the x axis, and by symmetry only one fourth of the domain ($y, z \geq 0$) was considered. The mesh was constructed by extrusion of a surface mesh having 50x50 quadrangles on each side of the cube, i.e. the mesh had 50x50x6/4= 3750 quadrangles on 1/4th of the cube. The mesh spacing was non-uniform, with a logarithmic refinement towards the edges of the cube, where the results show that large friction values are found. This refinement was such that the linear size h of the quadrangles near the center of the face was in a ratio 5:1 to the size near the edges. This surface mesh was extruded in the radial direction into 50 layers of hexahedral elements in the radial direction from the cube surface, up to an external cube of length $L_{\text{ext}} = 50$. The width of layers in the radial direction were also refined towards the internal cube surface in such a way that the width of the

external layer was in a ratio of 40:1 to the layer adjacent to the cube skin. Boundary conditions were $\mathbf{u} = (U_\infty, 0, 0)$ at inlet ($x = -L_{\text{ext}}/2$), $p = 0$ at outlet ($x = L_{\text{ext}}/2$), slip boundary condition at the lateral walls $y, z = \pm L_{\text{ext}}/2$, and non-slip boundary condition $\mathbf{u} = 0$ at the cube.

With this setup the computed value for the drag was $K = F_x/(\mu U_\infty L) = 13.76$. The numerical experiment was performed with other values of L_{ext} and mesh refinement in order to assess the sensibility of this result with respect to those parameters. This series of experiments have shown that this result is particularly sensitive to the size of the computational domain L_{ext}. This is so because the slip boundary conditions are equivalent to a lattice of mirrors of the cube with a spacing of $\Delta y = \Delta z = L_{\text{ext}}$. Then, each cube sees an *effective* external field given by U_∞ plus the velocity induced by the other cubes in the array. This field decays very slowly (as $O(1/L_{\text{ext}})$) for $L_{\text{ext}} \to \infty$, so that very large domains must be used in order to reduce the error. For instance, the error for $L_{\text{ext}} = 10$ is estimated in 15%. Computations for a sphere, for which the drag can be computed analytically show a similar behavior.

The result obtained with GBEM is 10% lower than the FEM value. This difference deserves some comments. Both results fall within the interval $(K_{\min}, K_{\max})$ predicted by analytic computations mentioned in section §4.3. In the GBEM computation the result is highly sensitive to the number of integration points, whereas for FEM the most influential parameter was the size of the computational domain. In both cases, some residual error may be due to insufficient mesh refinement. This is specially true in this case, because the strong variation of friction near the edges degrades convergence with respect to mesh refinement.

5 CONCLUSIONS

From the numerical simulations, when the number of panels is small, at least three and four Gauss-Legendre quadrature points in each integration coordinate were found to be necessary for a good approximation of the double surface integrals. This, in turn, implies a total of $3^4 = 81$ and $4^4 = 256$ integration points, respectively, for each pair of interacting panels. On the other hand, two points were nearly sufficient for meshes more refined, e.g. numerical simulations were also performed with 3072, 4800, 6912 and 9408 panels and two points. The system matrix obtained with a Galerkin technique remains full populated, as the most standard BEM schemes, but it is symmetric and positive defined.

Acknowledgments This work has received financial support from Consejo Nacional de Investigaciones Científicas y Técnicas (CONICET, Argentina, grants PIP 02552/00, PIP 5271/05), Universidad Nacional del Litoral (UNL, Argentina, grant CAI+D 2005-10-64) and Agencia Nacional de Promoción Científica y Tecnológica (ANPCyT, Argentina, grants PICT 12-14573/2003, PME 209/2003, PICT 1506/2006) and was partially performed with the *Free Software Foundation/ GNU-Project* resources as GNU/Linux OS, GNU/gfortran and GNU/Octave, as well as other Open Source resources as Scilab, MPICH, OpenDX, TGif and LaTeX.

REFERENCES

Becker A. *The Boundary Element Method in Engineering. A complete course*. Mc Graw Hill Book Co, 1992.

Burghignoli P., Pajewski L., Frezza F., and Galli A. Improved quadrature formulas for boundary integral equations with conducting or dielectric edge singularities. *IEEE Trans. on Antennas and Propagation*, 52(2):373–379, 2004.

D'Elía J. and Battaglia L. Integración numérica en ecuaciones integrales de superficie con

núcleos débilmente singulares y ponderadas por Galerkin. In Cardona, Nigro, Sonzogni, and Storti, editors, *Mecánica Computacional, vol. XXIV*, ISSN 1666-6070, pages 2861–2864. Santa Fe, 2006.

Eibert T.F. and Hansen V. On the calculation of potential integrals for linear source distributions on triangular domains. *IEEE Trans. on Antennas and Propagation*, 43(12):1499–1502, 1995.

Fachinotti V., Cardona A., D'Elía J., and Paquay S. BEM for the analysis of fluid flow around MEMS. In *Mecánica Computacional, vol. XXIV*, pages 1104–1119. 2007.

Hartmann F. *Introduction to Boundary Elements*. Springer-Verlag, 1989.

Kim S. and Karrila S.J. Integral equations of second kind for stokes flow: direct solutions for physical variables and removal of inherent accuracy limitations. *Chem. Eng. Comm.*, 82:123–161, 1989.

Ladyzhenskaya O. *The Mathematical Theory of Viscous Incompressible Flow*. Gordon and Breach Science Publishers, 2 edition, 1969.

Mikhlin S.G. *Multidimensional Singular Integrals and Integral Equations*. Pergamon Press, 1965.

Mikhlin S.G. *Mathematical Physics, An Advanced Course*. North-Holland, 1970.

Paquay S. *Développement d'une méthodologie de simulation numérique pour les problèmes vibro-acoustiques couplés intérieurs/extérieurs de grandes taille*. Ph.D. thesis, Faculté des Sciences Appliquees, Liege, 2002.

París F. and Cañas J. *Boundary Element Method. Fundamentals and applications*. Oxford Press, 1997.

PETSc-FEM. A general purpose, parallel, multi-physics FEM program, GNU General Public License, http://www.cimec.ceride.gov.ar/petscfem. 2007.

Power H. and Miranda G. Second kind integral equation formulation of stokes flows past a particle of arbitrary shape. *SIAM J. Appl. Math.*, 47(4):689–698, 1987.

Power H. and Wrobel L. *Boundary Integral Methods in Fluid Mechanics*. Computational Mechanics Publications, Southampton,UK, 1995.

Pozrikidis C. *Introduction to Theoretical and Computational Fluid Dynamics*. Oxford, 1996.

Pozrikidis C. *Boundary Integral and Singularity Methods for Linearized Viscous Flow*. Cambridge University Press, 1997.

Schuhmacher A. *Sound source reconstruction using inverse sound field calculations*. Ph.D. thesis, Departamente of Acoustic Technology, Technical University of Denamark, 2000.

Sievers D., Eibert T.F., and Hansen V. Correction to "On the calculation of potential integrals for linear source distributions on triangular domains". *IEEE Trans. on Antennas and Propagation*, 53(9):3113–3113, 2005.

Sonzogni V., Yommi A., Nigro N., and Storti M. Cfd finite element parallel computations on a beowulf cluster. In *ECCOMAS 2000*. 2000.

Taylor D.J. Accurate and efficient numerical integration of weakly singulars integrals in Galerkin IFIE solutions. *IEEE Trans. on Antennas and Propagation*, 51(7):1630–1637, 2003a.

Taylor D.J. Errata to "Accurate and efficient numerical integration of weakly singulars integrals in Galerkin IFIE solutions". *IEEE Trans. on Antennas and Propagation*, 51(9):2543–2543, 2003b.

Tezduyar T., Mittal S., Ray S., and Shih R. Incompressible flow computations with stabilized bilinear and linear equal order interpolation velocity-pressure elements. *Comp. Meth. App. Mech. Engng.*, 95:221–242, 1992.